University of Zurich
Physics Institute

Monte Carlo Simulation of the Liquid Xenon Detector Response to Low-Energy Neutrons

July 2, 2014

Bachelor Thesis of Dario Biasini
Supervisors:
Dr. Alexander Kish
Prof. Dr. Laura Baudis

Abstract

The relative scintillation yield $\mathcal{L}_{eff}$ is an important quantity characterising a detection medium. It is dependent on the energy deposit of the beam particle.
Several experiments have measured the scintillation yield to low-energy nuclear recoils in liquid xenon (figure 4).
Xurich II is a xenon two-phase detector designed to measure the yield at low recoil energies. At the time of writing this thesis, the experiment has not been done yet. Since the nuclear recoil energy is angle dependent, the experiment will be performed for a set of angles.
The goal of this bachelor thesis is to provide a Geant4 model of the experimental setup and to perform a first Monte Carlo simulation for a sample angle of 45°. As a cross check, the energy deposit is measured from the Monte Carlo Data. Furthermore, a collimator has been introduced to examine the collimation of the neutron beam. It has been found to be of no use. Additionally, a lead plate was placed in the beam's path to shield from background gammas. A lead thickness of 2 cm has been chosen.

Contents

1 Introduction **3**
- 1.1 Dark Matter . . . 3
- 1.2 Direct Search for Dark Matter in the XENON experiment . . . 4
- 1.3 Neutron Interactions . . . 5
- 1.4 Energy Scale . . . 6

2 Experiment **8**
- 2.1 The Xurich II Detector . . . 8
- 2.2 Principle of Measurement . . . 11

3 Implementation **12**
- 3.1 Geometry Setup . . . 12
- 3.2 Features . . . 15
- 3.3 Monte Carlo Simulation . . . 17
  - 3.3.1 Collimation . . . 17
  - 3.3.2 Gamma Shielding . . . 17
- 3.4 Full Simulation of the Measurement . . . 20
  - 3.4.1 Data Processing . . . 20
  - 3.4.2 Outcome of the Monte Carlo Experiment . . . 20
  - 3.4.3 Background . . . 22

4 Conclusions **23**

5 Acknowledgements **24**

1 Introduction

1.1 Dark Matter

Astronomical observations give rise to the assumption that most of the existing mass in the universe is not visible. This includes cosmic microwave background measurements [1], rotational velocity measurements of galaxy clusters [2] and gravitational lensing observations [3]. Only about 5% is luminous matter and therefore visible to telescopes [4]. To account for the missing mass, models suggest the existence of *dark matter*, that currently has only been detected indirectly through gravitational interaction with visible objects.

Although the exact nature of dark matter is still subject of research, WIMPs (**w**eakly **i**nteracting **m**assive **p**article) are promising candidates [5]. There exist several models that propose WIMP particles. One of the most prominent theories is *supersymmetry* [6], an extension to the standard model. Besides interacting gravitationally and weakly, WIMPs are predicted to be stable and electrically neutral. Additionally, they are considered to be non-relativistic (*cold* dark matter) [7] and predicted to interact with *nuclei* by weak interaction [6]. The current upper limit on the nucleon-WIMP cross section is seen in figure 1 with a minimum of $\sim 7.6 \cdot 10^{-46}$ cm^2 at a mass of 33 GeV/c^2 [8]. A lot of effort exists to detect WIMPs by non-gravitational means [9].

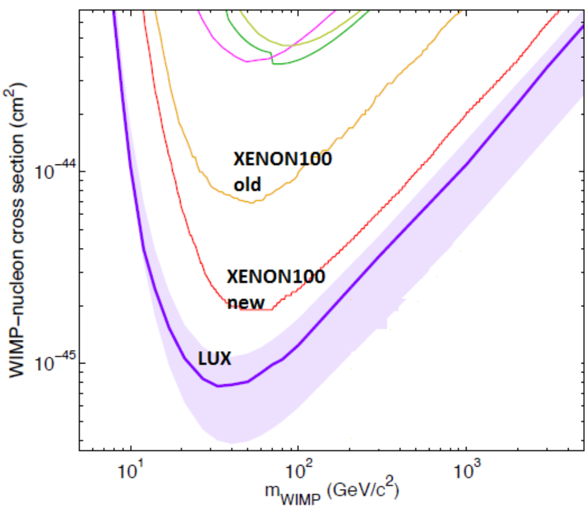

Figure 1: *current upper limits on the spin-independent elastic WIMP-nucleon scattering cross section* [8]
Experiments Large Underground Xenon (LUX) $\pm 1\sigma$ interval (violet), Edelweiss II (dark yellow line), CDMS II (green line), ZEPLIN-III (magenta line), XENON100 100 live-day (orange line, 'old'), and 225 live-day (red line, 'new') results

1.2 Direct Search for Dark Matter in the XENON experiment

The goal of the XENON collaboration is to measure the WIMP-nucleon cross section and the WIMP mass [10]. The predicted rate of interaction is in the order a few interactions per target ton per year for cross sections in the order of the current limit. The XENON experiment is located at the *Laboratori Nazionali del Gran Sasso* (Italy) 1400 meters underground to shield from cosmic rays. The experiment XENON100 uses liquid xenon (LXe) as a detection medium, measuring scintillation light and ionisation charge created by interaction of traversing particles. It has a liquid xenon mass of 161 kg, thereof 62 kg target mass, the rest representing the surrounding veto volume [11].

The detector is designed as a time projection chamber (TPC). Particles traversing the target may interact with the shell electrons or with the nucleus. This leads to ionisation, excitation as well as heat. The de-excitation of the shell and recombination of ionisation electrons with the xenon ions generate photons in the vacuum ultraviolet region ($\sim$ 178 nm) [12].

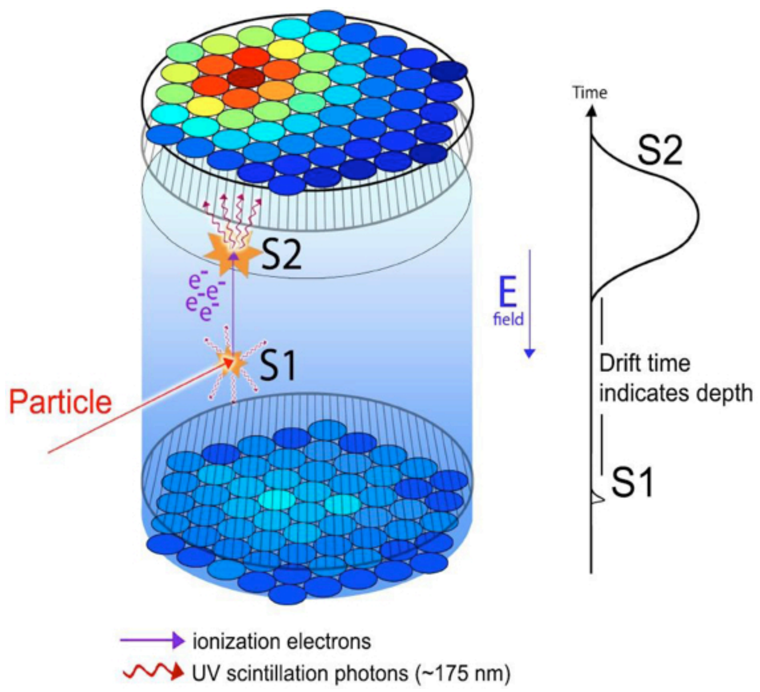

Figure 2: *mode of operation of a time projection chamber* [13]
The prompt signal S1 and the secondary signal S2 get detected by arrays of PMTs. The cathode is at a negative high voltage (HV), the gate in the middle is grounded. The anode is at a positive HV. The drift-time together with the electron's drift velocity indicates the z-position.

The immediate scintillation light signal (S1) is measured by 178 PMTs [11], distributed in two arrays at the top and bottom of the active volume(figure 2). Additionally, 64 PMTs are distributed in the veto for an anti-coincidence trigger. The ionised electrons that didn't recombine get separated from the ions by an electric field, generated by applying high voltage to the cathode. A second field created by applying high voltage to the anode at the top of the TPC extracts the electrons from the liquid into the gas phase. Collisions with xenon atoms in the gas phase induce the emission of secondary scintillation light (S2) proportional to the charge signal. By looking at the drift-time between S2 and S1, the z coordinate can be calculated. With the top array of PMTs, the (x,y) coordinate can be reconstructed, using a neural network algorithm and comparison with Monte Carlo simulations. The ratio of S2/S1 has different values for electronic and nuclear recoils [14]. This is used to discriminate the relevant signal from the electronic recoil background [15].

1.3 Neutron Interactions

Neutrons produce the same signal as expected of a WIMP i.e. the same ratio of S2/S1. They may scatter elastically or inelastically with the target nucleus. In inelastic scattering, the nucleus recoils and gets excited to higher energy states, resulting in de-excitation gammas of energies in the hundreds of keV up to MeV range. Furthermore, a neutron can get captured by a nucleus. Subsequently, light nuclei are emitted such as nucleons or alpha particles as well as gammas of energy up to tens of MeV. The cross section of neutrons decreases with increasing nucleon number of the target material.
The main energy depositing process is *elastic* scattering. The nuclear recoil energy for neutron elastic scattering E_r is given by theory as

$$E_r \approx 2E_n \frac{m_n M_{Xe}}{(m_n + M_{Xe})^2}(1 - \cos\theta), \tag{1}$$

where E_n is the incident neutron energy, m_n the neutron mass, m_{Xe} the xenon nucleus mass and θ the scattering angle (figure 3). Thus, one expects a recoil energy on the order of tens of keV for a neutron in in MeV range.

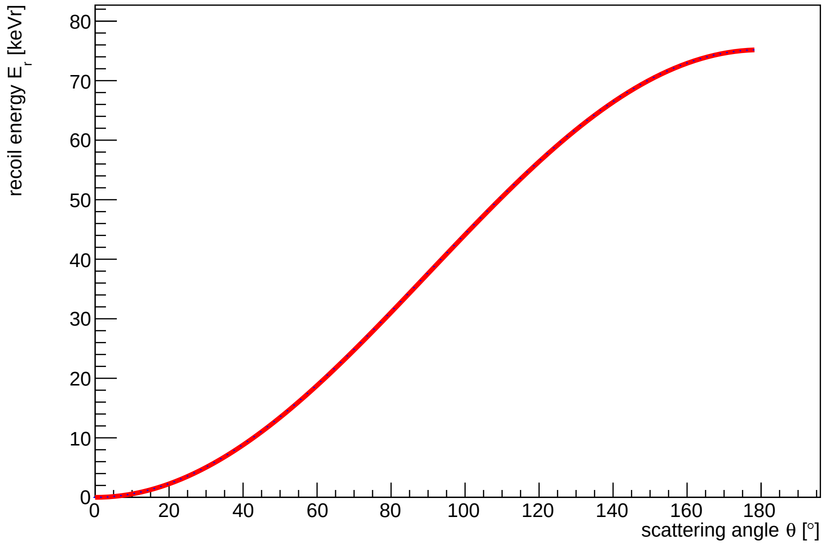

Figure 3: *nuclear recoil energy* in the range of 0 to 180 ° for a neutron energy of 2.45 MeV

1.4 Energy Scale

The scintillation yield, defined as the number of photons detected per unit energy, depends on the type of particle under consideration and is an energy dependent quantity. Only a fraction of the energy loss of a particle is converted into measurable photons [16]. The deposit also manifests itself as heat and ionisation, as mentioned. One defines the relative scintillation yield $\mathcal{L}_{eff}$ as the ratio of the scintillation yield of nuclear recoils to that of electronic recoils (L_y) from photoabsorbed 122 keV rays from a ^{57}Co source (at zero electric field) [17]. This has the advantage of being detector independent, absorbing any systematic errors connected to the setup.
$\mathcal{L}_{eff}$ is related to the nuclear recoil energy of single elastic neutron-nucleus scattering by [18]

$$\mathcal{L}_{eff}(E_{nr}) = \frac{S_{ee}}{S_{nr}} \frac{S1(E_{nr})}{E_{nr} L_y} \tag{2}$$

where $\frac{S_{ee}}{S_{nr}}$ is a quenching factor depending on the electric field ($S_{ee} \approx 0.5$ for electronic recoils and $S_{nr} \approx 0.9$ for nuclear recoils at a field of ≈ 0.7 kV/cm) [19], E_{nr} the nuclear recoil energy and L_y the reference light yield as described above.
It is conventional to use *keVr* for nuclear recoil energy to distinguish it from the electron equivalent recoil energy *keVee*.
Measurements of $\mathcal{L}_{eff}$ have already been performed (figure 4). This experiment will perform measurements of low recoil energies (small angles) and to reduce the

systematic uncertainties.

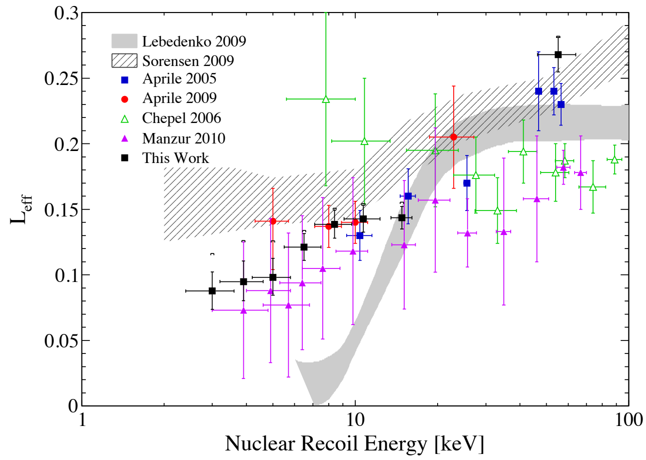

Figure 4: *Measured $\mathcal{L}_{eff}$ as of 2011*
'This Work' in the figure corresponds to its source paper [17].

In order to interpret the detector response (response means the measured signal of scintillation photons) and to relate it to recoil energies, Monte Carlo simulations are required. The uncertainty on the nuclear recoil energy is significantly affected by the geometry of the experimental setup. Thus, the simulations are also needed for an error estimation.

2 Experiment

2.1 The Xurich II Detector

Xurich I is a two-phase xenon TPC built to measure the scintillation and ionization yield of low-energy electronic recoils. The detector was also used to study energy calibrations with ^{83m}Kr photons [20]. Its successor Xurich II is built to study the light yield of low-energy neutrons in liquid xenon (LXe) at definite energies. Since neutrons, that only scatter once in the active volume, cannot be distinguished from WIMPs experimentally, they are suited to examine the properties of the xenon detector medium. It is much more compact than XENON100 with only two PMTs at the top and bottom of the target. Great effort was placed to reduce accidental scattering off non-sensitive material by reducing the amount of material used.
A CAD model of the Xurich II detector is shown in figure 5.
The target liquid xenon volume lies inside the drift spacer (4). Its interior has a height of 28 mm and a diameter of 17.5 mm. At the bottom of the drift spacer lies the cathode (3) with a copper-beryllium wire mesh. The drift field needed to drift the electrons upward extends up to the grounded gate, followed by a stronger electric field to the anode to accelerate the electrons and to get secondary scintillation light (S2). The drift spacer is surrounded by copper wire rings that ensure a uniform electric field. The field values can be adjusted during operation. The drift field will be on the order of kV/cm [21]. The drift velocity of electrons in liquid xenon is approximately $2 \cdot 10^5$cm s^{-1} at 1 kV/cm electric field voltage.

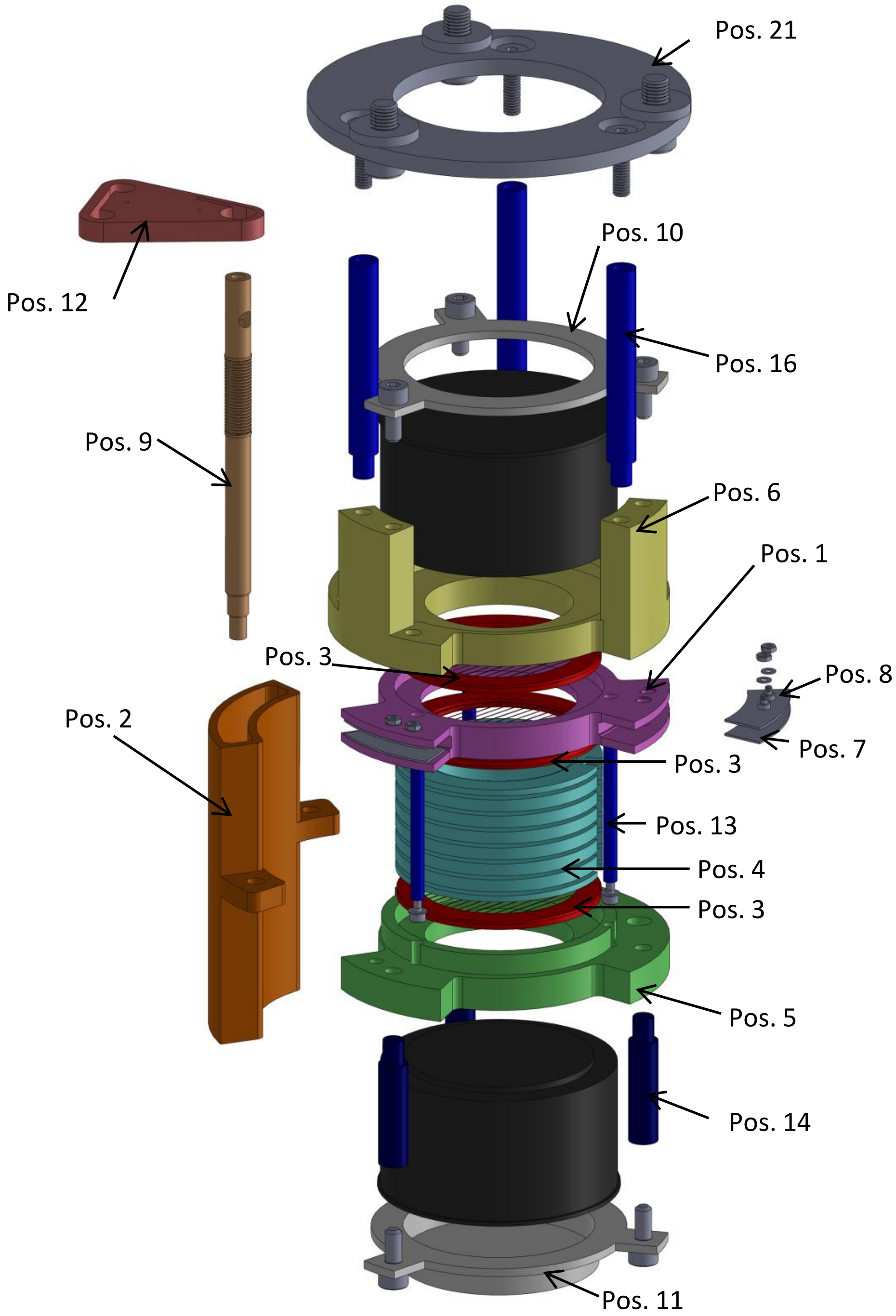

Figure 5: *CAD model of the TPC*, the most relevant parts are:
(1) grid holder, (2) level-control cup, (3) cathode (bottom), gate (middle) and anode (top), (4) drift spacer (active volume), (7) capacitor plates, (9) level-control pipe with bellow, (black cylinders) PMTs

The liquid xenon level resides between the grid and the cathode in (1). It can be varied in a range of 0.9 mm. By measuring the capacitance between the plates (7), the liquid xenon level can be determined with μm precision. The top part of the TPC is surrounded by gaseous xenon. The level-control pipe (9) has a built-in bellow to regulate the xenon height. Xenon first spills into the level-control cup (2), that allows for a smooth level adjustment of the liquid surface. There are two 2″-diameter Hamamatsu R9869/R6041 PMTs located at the top and bottom [22]. The TPC has a total height of 170 mm and a diameter of 90 mm. All parts but the level control components (brass) and steel holders (11/12) are made out of PTFE (Polytetrafluoroethylene, known as Teflon). PTFE has suitable insulator properties and is a good reflector for the VUV scintillation light. The cooling to operating temperature shrinks PTFE by about 1.5% [11].
The LXe temperature is held at a constant temperature of 175 K and a pressure of 1.8 bar by a specifically designed vacuum cryostat. The cooling is provided by a copper finger immersed in a liquid nitrogen bath. Utility pipes for electrical wiring, pumps and inlet/outlets for Xe circulation are attached to the top flange [20].

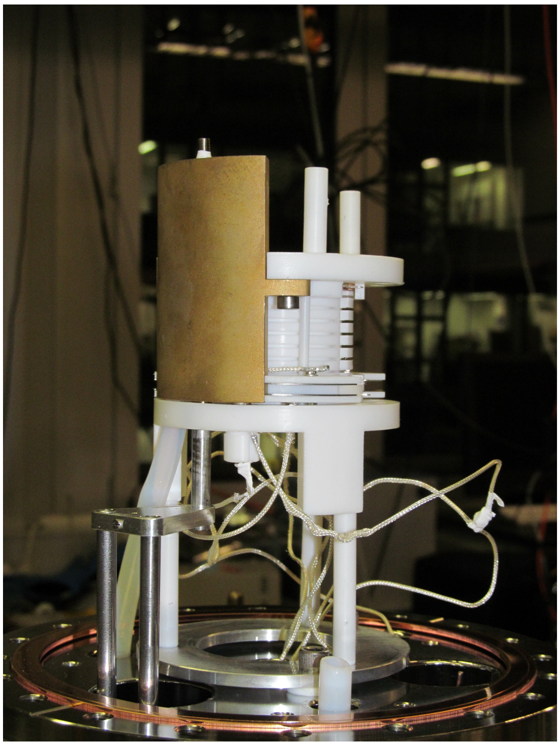

Figure 6: *The Xurich II TPC during its assembly.*

2.2 Principle of Measurement

The main goal of the experiment is to measure $\mathcal{L}_{eff}$ of liquid xenon at low recoil energies. The recoil energy distribution of neutrons scattered elastically at an angle θ with respect to the beam axis (figure 8) is simulated. Two organic scintillators will detect the scattered neutrons leading to an energy selection criterion (equation 1).

The detector is placed in front of the exit of the NSD-1e7-DD-C neutron generator by NSD-Fusion GmbH. It provides a monoenergetic beam of neutrons with a kinetic energy of 2.45 MeV produced by deuterium-deuterium fusion. It has a measured Neutron flux of $1.25 \cdot 10^5 \mathrm{s}^{-1}$ according to manufacturer (at 1% of the maximum flux, which will be the main operating mode) [23].

$$^2\mathrm{H} +^2 \mathrm{H} \rightarrow^3 \mathrm{He}(0.82\ \mathrm{MeV}) + \mathrm{n}(2.45\ \mathrm{MeV}) \tag{3}$$

The NSD Neutron Generator consists of a reaction chamber which is housed in a aluminum cylinder. The source is enclosed by a borated polyethylene shield and a concrete block. The neutrons exit through a 100 mm diameter window. The organic liquid scintillator detectors are 3″ diameter Eljen Technologies M510 detectors filled with EJ301. EJ301 is especially adapted to fast neutron detection in the presence of γ radiation due to its excellent pulse shape discrimination (PSD) characteristics [17].

The neutrons are generated isotropically in the generator volume. The goal is to obtain a beam of small cross section, definite energy and small angular spread. The effect of two types of collimators is analysed (figure 7) in three sample configurations. They have a shape of a cylinder with a conical hole in the middle, the material is chosen to be polyethylene.

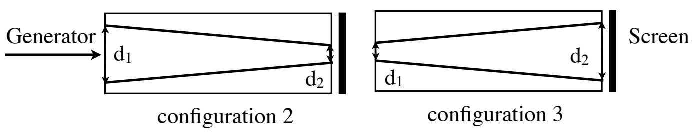

Figure 7: *schematic cut through the collimator in configuration 2 and 3*
Configuration one is without a collimator. The *screen* is where the particles get registered in the simulation.

3 Implementation

The code was written in Geant4.9.6.2 [24] using ROOT 5.34.10 [25] as an analysis tool. A photon counter is implemented for the PMTs, but not used in this simulation. The photon response can in principle be simulated with Geant4, but a different physics implementation would be needed for proper scintillation. Additionally, there exists an option to make every material/volume in the setup active, such as the generator enclosure or the cryostat.

3.1 Geometry Setup

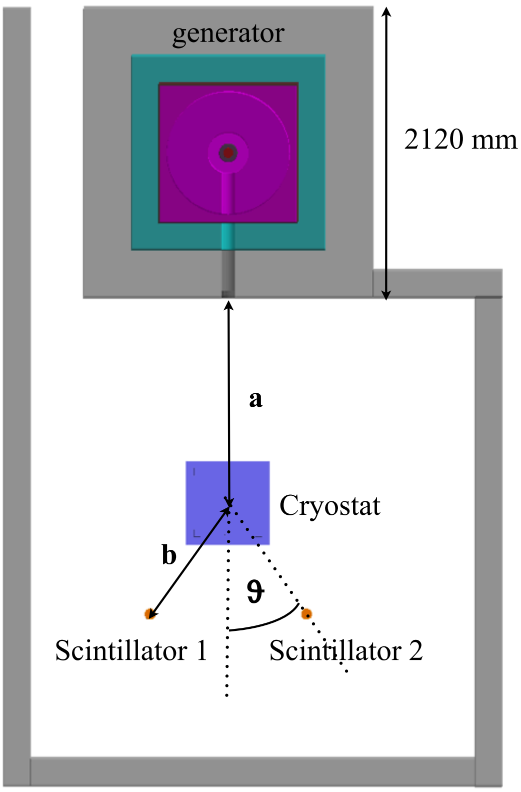

Figure 8: *experimental setup*
The generator part constists of a concrete block (grey), containing a borated polyethylene (BPE) neutron shield (cyan) and a paraffin container (magenta). The cryostat is cylindrical, seen is only the quadratic base plate.

First, the particles are tracked at a virtual screen of 1 μm thickness just after the collimator. The simulation was performed for three configurations, that are configuration 1 without a collimator, r_1=50 mm and r_2=15 mm for configuration 2, and r_1=15 mm and r_2=50 mm for configuration 3.

A sample of primary particles is recorded at screen position for a suitable collimation and gamma shielding configuration. The cryostat is placed at a distance $a = 1$ m from the generator exit. The scintillators are placed at an angle θ and at a distance $b = 1$ m from the cryostat. The height of the cryostat is adjusted to $z = 1.1$ m, such that the center of the neutron beam hits the center of the active volume. Figure 3.1 shows the Geant4 model of the Cryostat, figure 3.1 the model of Xurich II.

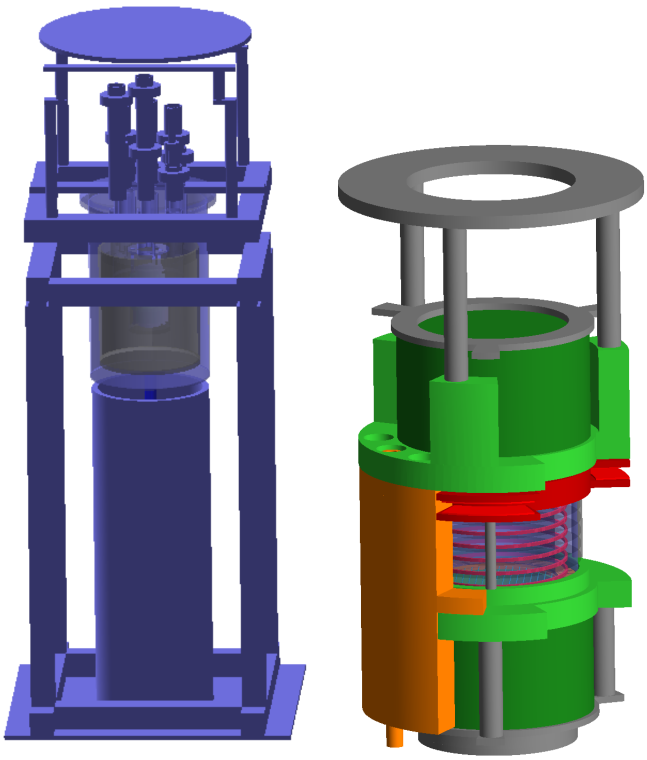

(a) cryostat (b) TPC

Figure 9: *Geant4 models of the (a) cryostat and (b) TPC* (colors and transparencies just for visualisation purposes)
(a) One can see the (here transparent) vacuum aluminium can containing the TPC (grey)
(b) The xenon spills into the brass cup (orange). The target resides in the drift spacer (transparent blue). The PMTs are coloured in dark green.

Inside the TPC, there are several sensitive volumes, as shown in figure 10. The layer of liquid between cathode and bottom PMT is charge insensitive, since it is outside of the drift field. A photon scattering once in region 2 or 3 and once in region 1 might get confused as a nuclear recoil event. It can be excluded by a cut in the z-coordinate. Regions 4 and 5 contain gaseous xenon, thus only volumes 2 and 3 are considered to be active. The information recorded in these volumes includes the energy, position, time, type of particle, creation processes and energy depositing process.

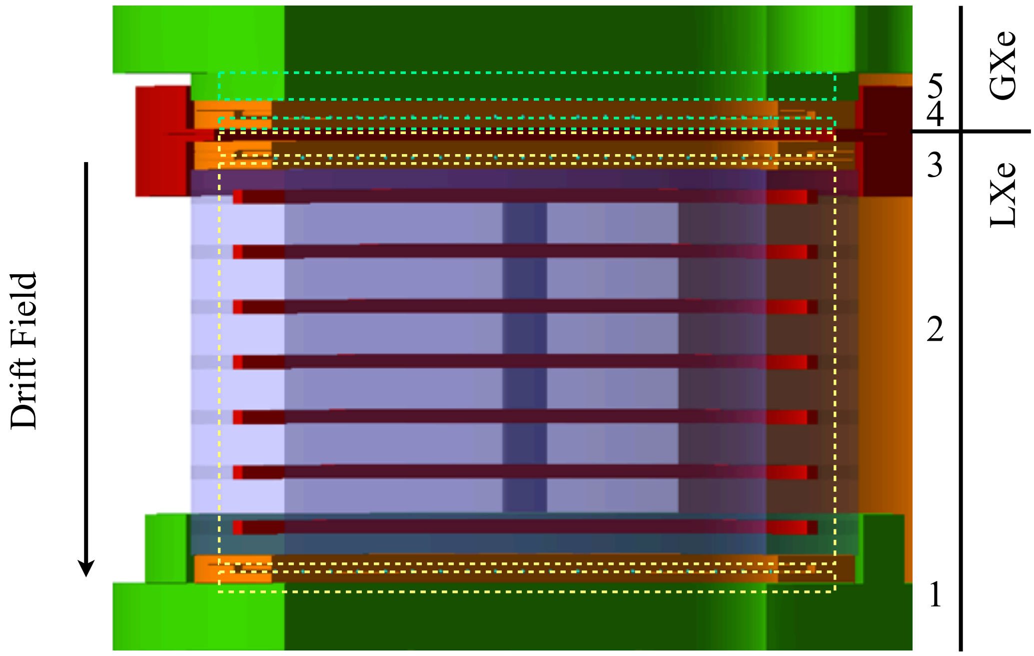

Figure 10: *labeling on the TPC sensitive regions*
The numbers correspond to the code internal numbering of the xenon active regions, that is stored in the output file.

3.2 Features

The code provides a set of user interface commands. Apart from visualisation options, one may

- enable/disable the use of a collimator
- set the two inner radii of the collimator
- set the material of the collimator
- set the length of the collimator
- set the angle of the organic scintillators
- choose from primary generators *neutron generator*, *particle gun* or *screen source*
- define various variables for particle source control such as setting the energy, particle type, direction, distribution etc.
- toggle between *normal mode* and *screen mode* to activate/deactivate sensitive detectors
- toggle *general mode* to make every volume sensitive
- the hadronic physics list

The primary generators provided includes a neutron generator, as described above, featuring a monoenergetic isotropic distribution of neutrons with an energy of 2.45 MeV and a Geant4 built-in particle gun, consisting of a simple beam of definite direction with no randomization. Additionally, the screen particle source is designed to take input from a *.root* file filled with particles at screen position and convert them into primaries. It reades out a random particle from the file for each event. The information registered is the type of particle (gamma or neutron), momentum, energy and position.
The hadronic physics list can be chosen from the predefined QGSP_BERT (QGSP stands for **q**uark-**g**luon **s**tring **p**recompound [26]) for fast test calculations, and QGSP_BERT_HP as well as QGSP_BIC_HP for high neutron transport precision in the actual run. These are recommended physics lists that are well suited for low-energy neutron simulations [27]. The last two differ by the hadronic cascade model used (Bertini cascade and binary cascade respectively). The addition of HP adds high precision data for a precise transportation of neutrons below 20 MeV.

In the source code, one can change easily

- the liquid xenon level between gate and anode
- the electromagnetic physics list

The program can be evoked with command line options

- -o [path to output file]
- -f [path to run macro]
- -i [path to initalization macro]
- -s [path to screen input files]
- -i interactive mode
- -v visualisation mode
- -n [number] run with a number of n events

A macro to merge the screen output to input files for the main simulation exists in addition to the Geant4 source code. Additional code may be used to analyse the simulation for an arbitrary configuration.

3.3 Monte Carlo Simulation

3.3.1 Collimation

The collimation has been simulated for 10^7 events per configuration. This corresponds to a lifetime of 80 seconds. Figure 11 shows the relevant histograms.

configuration	rate [s^{-1}]	mean energy [MeV]	mean p_z/p	γ to n ratio [%]
1: without collimator	119.6±1.2	1.84±0.009	0.974±0.001	37±0.9
2: $r_1 = 50$ mm, $r_2 = 15$ mm	12.1±0.4	1.57±0.03	0.923±0.005	112±5
3: $r_1 = 15$ mm, $r_2 = 50$ mm	30.7±0.6	1.76±0.02	0.967±0.002	75±2

In conf. 3, the angular spread is ≈ 18 mm as opposed to the collimator inner radius of 15 mm. Comparing conf. 3 to conf. 1, the rate of 2.45 MeV neutrons (highest bin) is reduced by about one order of magnitude, the rate of lower energy neutrons (energy < 2 MeV) does not change significantly. For both types of collimators, one can note that the neutron rate decreases notably when introducing a collimator. As a side effect, a number of unwanted gammas get produced.

3.3.2 Gamma Shielding

In practice, it is not always possible to distinguish between electronic and nuclear recoil. Some signals might overlap, covering relevant peaks that the readout software cannot tag. Therefore, it is necessary to reduce the electronic recoil background. To decrease the gamma rate, a plate of high-Z material can be placed at the exit of the generator. This setup is simulated for a lead plate with thicknesses ranging from 0 to 5 cm in 1 cm steps.
A number of 10^8 events has been simulated for each configuration. Figure 12 shows the relevant data. Looking at the number of neutrons with an energy higher than 2.4 MeV, one clearly wants a minimum thickness of lead. On the other hand, a minimum ratio of gamma to neutron rate is required. Note, that at ~ 2 cm the ratio of gammas to neutrons is reaching a constant value.

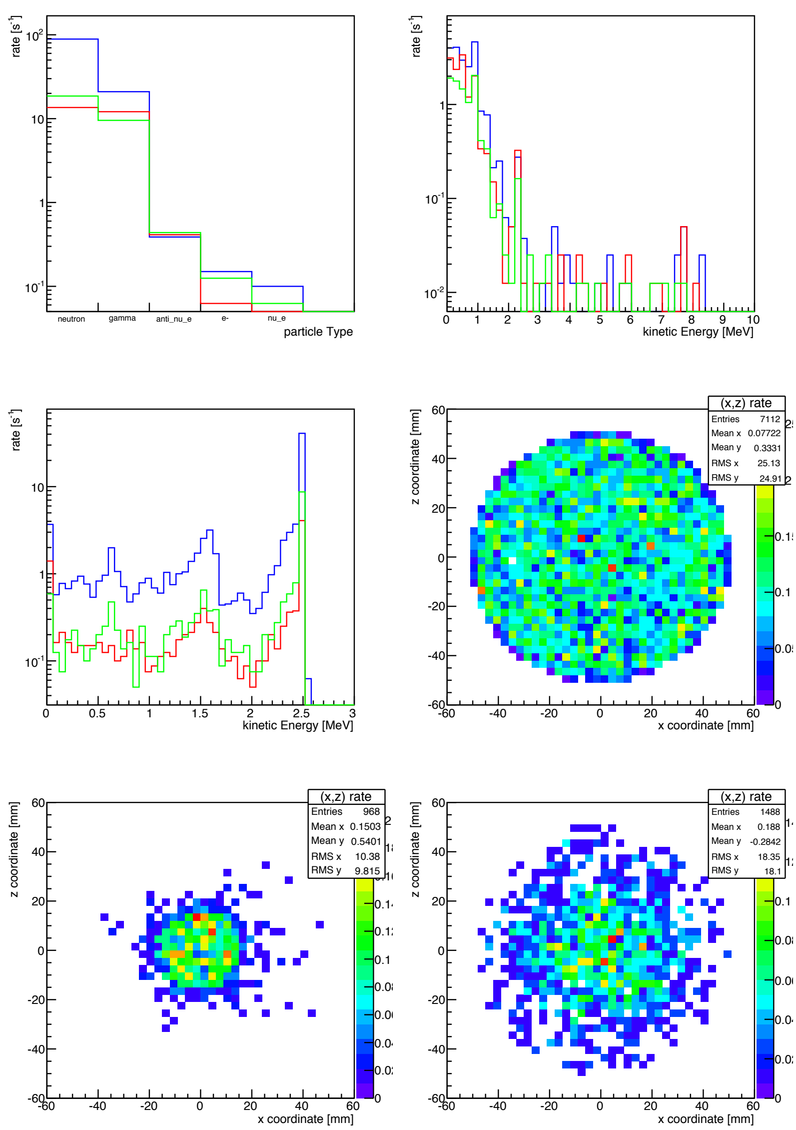

Figure 11: *data output for collimation tracked at the virtual screen* (from left to right, top to bottom)
color coding: conf. 1 (blue), conf. 2 (red) and conf. 3 (green)
The first histogram shows the rate of particles detected at screen position for the three configurations. The second histogram shows the kinetic energy distribution for gammas, the third for neutrons.
The other three plots show the neutron rate [s^{-1}] in conf. 1-3 at the screen (x,z) plane.

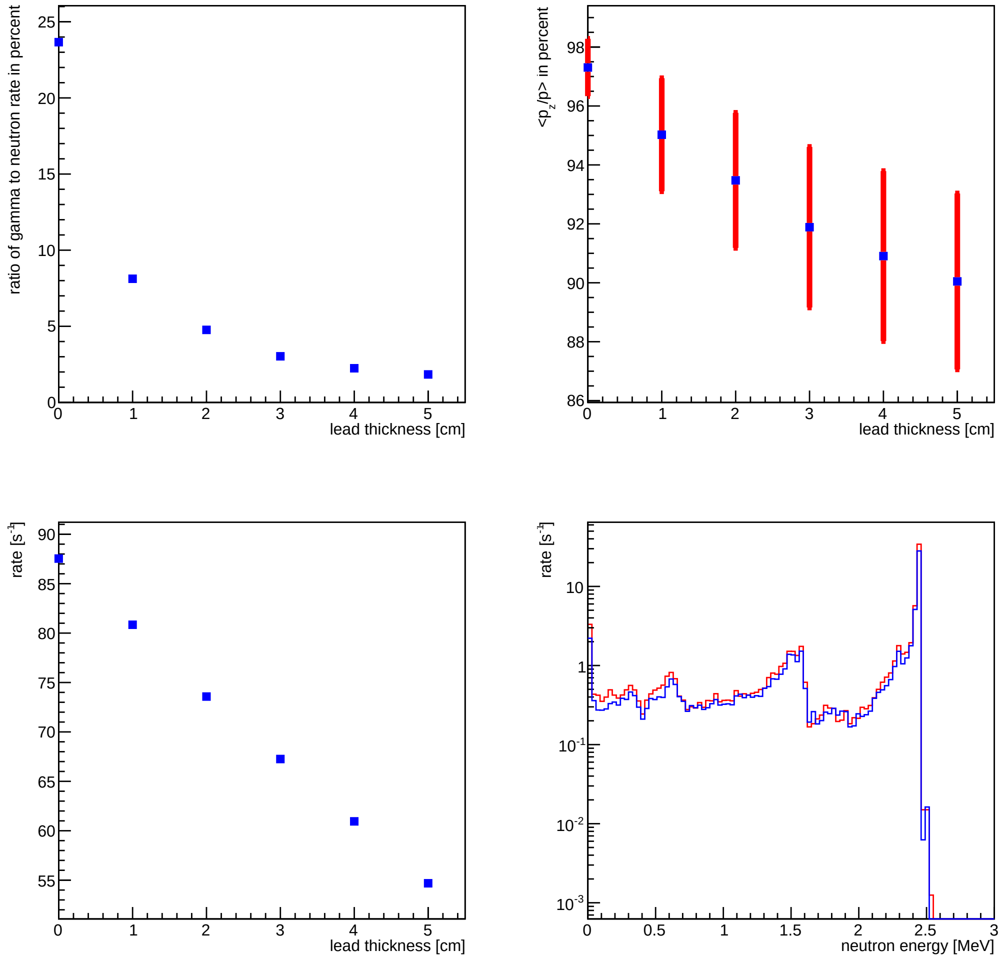

Figure 12: *screen output for gamma shielding as a function of lead thickness* (from left to right, top to bottom)
The first plot shows the ratio of gamma/neutron rate in percent, the second the mean p_z/p, the third graph shows the neutron rate.
In the last plot, one can see the energy distributions of the neutrons for a lead thickness of 0 cm (red) and 3 cm (blue). The statistical error bars not shown here are too small to be visualised.

3.4 Full Simulation of the Measurement

Following the previous considerations, configuration 1 and a lead plate of 2 cm is chosen. A set of 10^9 events is sampled at the screen position for further use. The coincidence of an energy deposit in one of the scintillators and the active liquid xenon volume serves as a trigger. The liquid xenon level is set to 4.5 mm relative to the bottom of the grid holder in figure 5.

3.4.1 Data Processing

Since the detector has a finite position resolution, not all energy deposits for an interacting neutron can be told apart. The time difference between two S2 peaks must be greater than 2 μs for a successful readout. The minimal z-distance has been measured to be 3 mm in average. This distance depends on the drift velocity and on the readout software.
Taking this into account, the energy depositing events in the TPC are first ordered by height z. Beginning with the topmost, the energy deposits get written to a histogram. Additionally, if the neutron didn't deposit energy in any material other than the active liquid xenon and the scintillator, the event is considered as *true coincidence*. The data can further be refined, by applying a time-of-flight cut. This excludes slower neutrons that scattered in other materials and contribute to background. To figure out at which time to cut, the time-of-flight is evaluated with a single collinear beam of definite neutron energy 2.45 MeV.

3.4.2 Outcome of the Monte Carlo Experiment

Figure 13 shows the time-of-flight (TOF) and energy deposition distributions in the liquid xenon for a sample angle of 45 degrees and a number of 10^7 events. Electronic recoils are excluded in this analysis. A TOF cut of 50 ns is chosen, such that the peak is fully contained in this region. A more precise cut value results in less contamination of the data, resulting in a smoother distribution. A more precise positioning of the cut value is thus not relevant. For generator neutrons as a primary source, the results are as shown in figure 14. A number of 10^8 events has been simulated.

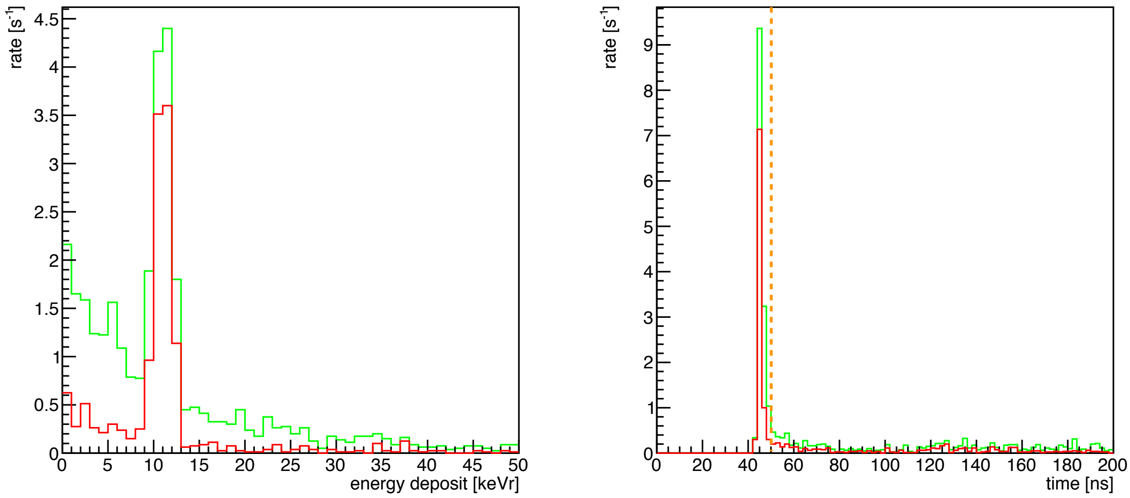

Figure 13: *sample output for a neutron beam of energy 2.45 MeV and energy deposit in LXe*
nuclear recoil (green), true coincidence (red), TOF cut (dashed orange line)

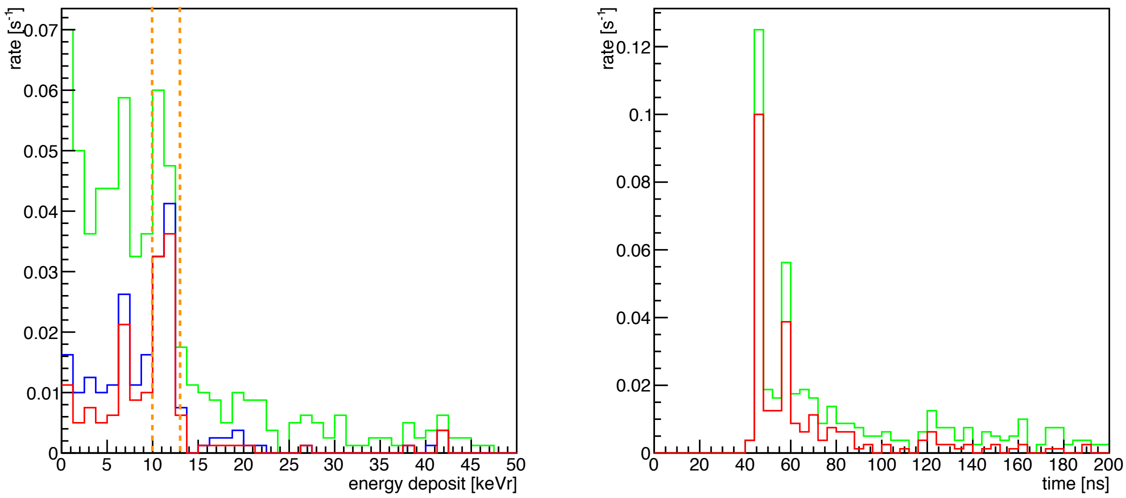

Figure 14: *sample output for a neutron beam of energy 2.45 MeV*
nuclear recoil (green), TOF cut (blue), true coincidence (red), energy interval for calculating the mean value and deviation (dashed orange lines)

The peak is clearly visible and can be taken to calculate the mean recoil energy as well as the standard deviation. This corresponds to (11.1 ± 0.1) keVr. The predicted value of 11.0 keVr is well within the error range.

3.4.3 Background

Events outside of peak on the left in figure 14 originate from neutron inelastic scattering with energy deposits of the recoiling xenon atoms comparable to the elastic scattering deposits or from neutrons with additional deposits in non-active material.
Neutrons travelling directly from the generator to the scintillators are excluded by requiring coincidence, slow neutrons (as in conf. 1 of figure 11) get excluded by the TOF cut.
Gammas originating from neutron capture may have energies higher than 2.45 MeV (up to 10 MeV). Figure 15 shows the materials responsible for neutron capture and inelastic scattering. For neutron capture, concrete is the most relevant material, inelastic scattering happens mainly in concrete, steel and aluminium.

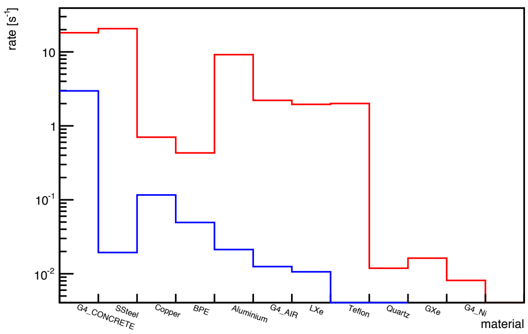

Figure 15: *inelastic scattering (red) and neutron capture (blue) rate* sorted by material

For inelastic scattering, Geant keeps track of the resulting xenon isotopes. It is interesting to look at their relative distribution.

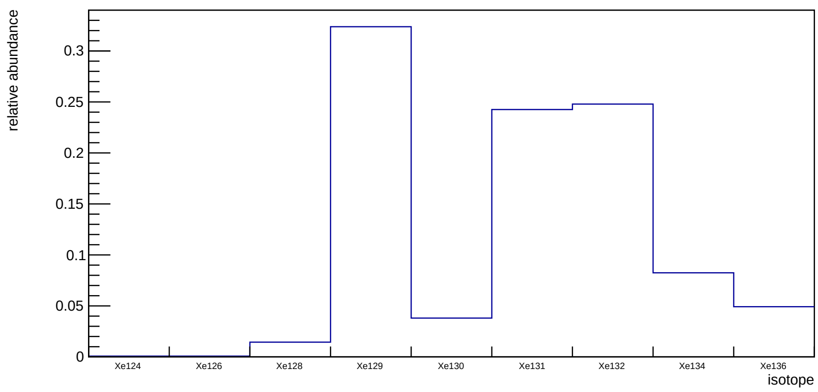

Figure 16: *distribution of the xenon isotopes after inelastic scattering*

4 Conclusions

In the course of this bachelor thesis, several tasks have been accomplished. A sample simulation of 45° has been performed. The simulations based on this code will be continued by the group. They will be performed with a much higher number of events and for a set of angles, corresponding to the measured angles in the experiment. As a conclusion, the key accomplishements are listed here.

- In the scope of this thesis, a Geant4 model for the Xurich II experiments has been developed.
- A suitable user interface is provided for further simulations.
- The predicted curve of the nuclear recoil energy is well within the error of the simulated data.
- The use of different types of neutron collimators has been simulated and was found to be of no relevance.
- Gammas have been found to originate from inelastic scattering and neutron capture. Neutron capture is mostly found in aluminium, steel and concrete, inelastic scattering in concrete.
- Gamma shielding has been examined by introducing lead plates and compared for different thicknesses. A lead shield with thicknesses of 2 cm has been chosen for the experiment.

5 Acknowledgements

I would like to thank Dr. Alexander Kish for his incredible help, patience and time invested on teaching me. I would also like to thank Prof. Dr. Laura Baudis for making this bachelor project possible. Additionally, I'd like to thank Francesco Piastra for showing me how to simulate on the cluster.

List of Figures

1 *current upper limits on the spin-independent elastic WIMP-nucleon scattering cross section* [8]
Experiments Large Underground Xenon (LUX) $\pm 1\sigma$ interval (violet), Edelweiss II (dark yellow line), CDMS II (green line), ZEPLIN-III (magenta line), XENON100 100 live-day (orange line, 'old'), and 225 live-day (red line, 'new') results 3
2 *mode of operation of a time projection chamber* [13]
The prompt signal S1 and the secondary signal S2 get detected by arrays of PMTs. The cathode is at a negative high voltage (HV), the gate in the middle is grounded. The anode is at a positive HV. The drift-time together with the electron's drift velocity indicates the z-position. 4
3 *nuclear recoil energy* in the range of 0 to 180 ° for a neutron energy of 2.45 MeV 6
4 *Measured $\mathcal{L}_{eff}$ as of 2011*
'This Work' in the figure corresponds to its source paper [17]. . . . 7
5 *CAD model of the TPC*, the most relevant parts are:
(1) grid holder, (2) level-control cup, (3) cathode (bottom), gate (middle) and anode (top), (4) drift spacer (active volume), (7) capacitor plates, (9) level-control pipe with bellow, (black cylinders) PMTs 9
6 *The Xurich II TPC during its assembly.* 10
7 *schematic cut through the collimator in configuration 2 and 3*
Configuration one is without a collimator. The *screen* is where the particles get registered in the simulation. 11
8 *experimental setup*
The generator part constists of a concrete block (grey), containing a borated polyethylene (BPE) neutron shield (cyan) and a paraffin container (magenta). The cryostat is cylindrical, seen is only the quadratic base plate. 12

9 *Geant4 models of the (a) cryostat and (b) TPC* (colors and transparencies just for visualisation purposes)
(a) One can see the (here transparent) vacuum aluminium can containing the TPC (grey)
(b) The xenon spills into the brass cup (orange). The target resides in the drift spacer (transparent blue). The PMTs are coloured in dark green. 13
10 *labeling on the TPC sensitive regions*
The numbers correspond to the code internal numbering of the xenon active regions, that is stored in the output file. 14
11 *data output for collimation tracked at the virtual screen* (from left to right, top to bottom)
color coding: conf. 1 (blue), conf. 2 (red) and conf. 3 (green)
The first histogram shows the rate of particles detected at screen position for the three configurations. The second histogram shows the kinetic energy distribution for gammas, the third for neutrons.
The other three plots show the neutron rate [s^{-1}] in conf. 1-3 at the screen (x,z) plane. 18
12 *screen output for gamma shielding as a function of lead thickness* (from left to right, top to bottom)
The first plot shows the ratio of gamma/neutron rate in percent, the second the mean p_z/p, the third graph shows the neutron rate.
In the last plot, one can see the energy distributions of the neutrons for a lead thickness of 0 cm (red) and 3 cm (blue). The statistical error bars not shown here are too small to be visualised. 19
13 *sample output for a neutron beam of energy 2.45 MeV and energy deposit in LXe*
nuclear recoil (green), true coincidence (red), TOF cut (dashed orange line) 21
14 *sample output for a neutron beam of energy 2.45 MeV*
nuclear recoil (green), TOF cut (blue), true coincidence (red), energy interval for calculating the mean value and deviation (dashed orange lines) 21
15 *inelastic scattering (red) and neutron capture (blue) rate* sorted by material 22
16 *distribution of the xenon isotopes after inelastic scattering* 22

References

[1] Aravind Natarajan. A closer Look at CMB Constraints on WIMP Dark Matter. 2012. http://arxiv.org/abs/1201.3939 arXiv:1201.3939.

[2] Fritz Zwicky. Spectral displacement of extra galactic nebulae. *Helv. Phys. Acta.*, 6:110–127, 1933.

[3] Richard Massey, Thomas Kitching, and Johan Richard. The dark matter of gravitational lensing. *Rept.Prog.Phys.*, 73:086901, 2010. http://arxiv.org/abs/1001.1739 arXiv:1001.1739, http://dx.doi.org/10.1088/0034-4885/73/8/086901 doi:10.1088/0034-4885/73/8/086901.

[4] N. Jarosik et al. Seven-Year Wilkinson Microwave Anisotropy Probe (WMAP) Observations: Sky Maps, Systematic Errors, and Basic Results. 2010. http://arxiv.org/abs/1001.4744 arXiv:1001.4744.

[5] Jonathan L. Feng. Dark Matter Candidates from Particle Physics and Methods of Detection. *Ann.Rev.Astron.Astrophys.*, 48:495–545, 2010. http://arxiv.org/abs/1003.0904 arXiv:1003.0904, http://dx.doi.org/10.1146/annurev-astro-082708-101659 doi:10.1146/annurev-astro-082708-101659.

[6] Gerard Jungman, Marc Kamionkowski, and Kim Griest. Supersymmetric dark matter. *Phys.Rept.*, 267:195–373, 1996. http://arxiv.org/abs/hep-ph/9506380 arXiv:hep-ph/9506380, http://dx.doi.org/10.1016/0370-1573(95)00058-5 doi:10.1016/0370-1573(95)00058-5.

[7] Cristian Armendariz-Picon and Jayanth T. Neelakanta. How Cold is Cold Dark Matter? 2013. http://arxiv.org/abs/1309.6971 arXiv:1309.6971.

[8] D.S. Akerib et al. First Results from the LUX Dark Matter Experiment at the Sanford Underground Research Facility. page 5, 2013. http://arxiv.org/abs/1310.8214 arXiv:1310.8214.

[9] Katherine Garrett and Gintaras Duda. Dark Matter: A Primer. *Adv.Astron.*, 2011:968283, 2011. http://arxiv.org/abs/1006.2483 arXiv:1006.2483, http://dx.doi.org/10.1155/2011/968283 doi:10.1155/2011/968283.

[10] XENON Collaboration. The XENON Dark Matter Project, Dec 2013. URL: http://xenon.astro.columbia.edu.

[11] E. Aprile et al. The XENON100 Dark Matter Experiment. *Astropart.Phys.*, 35:573–590, 2012. http://arxiv.org/abs/1107.2155 arXiv:1107.2155, http://dx.doi.org/10.1016/j.astropartphys.2012.01.003 doi:10.1016/j.astropartphys.2012.01.003.

[12] M. Szydagis et al. NEST: A Comprehensive Model for Scintillation Yield in Liquid Xenon. http://arxiv.org/abs/1106.1613 arXiv:1106.1613.

[13] image from LUX homepage, Dec. 2013. URL: http://lux.physics.ucdavis.edu/glossary/tpc.php.

[14] E. Aprile, C. E. Dahl, L. de Viveiros, R. J. Gaitskell, K. L. Giboni, J. Kwong, P. Majewski, K. Ni, T. Shutt, and M. Yamashita. Simultaneous Measurement of Ionization and Scintillation from Nuclear Recoils in Liquid Xenon for a Dark Matter Experiment. *Phys. Rev. Lett.*, 97:081302, Aug 2006. URL: http://link.aps.org/doi/10.1103/PhysRevLett.97.081302, http://dx.doi.org/10.1103/PhysRevLett.97.081302 doi:10.1103/PhysRevLett.97.081302.

[15] XENON 100 Collaboration. The XENON100 Dark Matter Experiment. 2013. http://arxiv.org/abs/1301.6620v2 arXiv:1301.6620v2.

[16] CERN collaboration. Cern Particle Detector BriefBook, Nov. 2013. URL: http://www.cern.ch/RD11/rkb/PH14pp/node100.html.

[17] G. Plante, E. Aprile, R. Budnik, B. Choi, K.L. Giboni, et al. New Measurement of the Scintillation Efficiency of Low-Energy Nuclear Recoils in Liquid Xenon. *Phys.Rev.*, C84:045805, 2011. http://arxiv.org/abs/1104.2587 arXiv:1104.2587, http://dx.doi.org/10.1103/PhysRevC.84.045805 doi:10.1103/PhysRevC.84.045805.

[18] W. Mu, X. Xiong, and X. Ji. Scintillation Efficiency for Low-Energy Nuclear Recoils in Liquid-Xenon Dark Matter Detectors. 2013. http://arxiv.org/abs/1306.0170 arXiv:1306.0170.

[19] W.-M.Yao et al. New Measurement of the Scintillation Efficiency of Low-Energy Nuclear Recoils in Liquid Xenon. *J.Phys.*, G33, 2006.

[20] A. Manalaysay, T.M. Undagoitia, A. Askin, L. Baudis, A. Behrens, et al. Spatially uniform calibration of a liquid xenon detector at low energies using ^{83m}Kr. *Rev.Sci.Instrum.*, 81:073303, 2010. http://arxiv.org/abs/0908.0616 arXiv:0908.0616, http://dx.doi.org/10.1063/1.3436636 doi:10.1063/1.3436636.

[21] H. Dujmovic. Simulation and Optimization of the Electric Field in a Liquid Xenon Time Projection Chamber. 2012. Bachelor's thesis.

[22] Laura Baudis, Hrvoje Dujmovic, Christopher Geis, Andreas James, Alexander Kish, et al. Response of liquid xenon to Compton electrons down to 1.5 keV. *Phys.Rev.*, D87:115015, 2013. http://arxiv.org/abs/1303.6891 `arXiv:1303.6891`, http://dx.doi.org/10.1103/PhysRevD.87.115015 `doi:10.1103/PhysRevD.87.115015`.

[23] A. Aeschbacher. Simulation of a Neutron Generators Radiation Shield. 2010. Bachelor's thesis.

[24] S. Agostinelli et al. Geant4 A Simulation Toolkit. *Nuclear Instruments and Methods A*, 506:250–303, 2003.

[25] Rene Brun and Fons Rademakers. ROOT - An Object Oriented Data Analysis Framework. *Nucl. Inst. Meth. in Phys. Res. A*, 389:81–86, 1997.

[26] Nov. 2013. URL: `http://geant4.cern.ch/support/proc_mod_catalog/models/hadronic/QGSP.html`.

[27] Nov. 2013. URL: `http://geant4.cern.ch/support/proc_mod_catalog/physics_lists/referencePL.shtml`.